Ab Initio Study of the Radii of Oxygen Isotopes

Zhengxue Ren[1,2,3,*] Serdar Elhatisari[4,5,†] and Ulf-G. Meißner[2,1,6,‡]

[1]*Institute for Advanced Simulation (IAS-4), Forschungszentrum Jülich, D-52425 Jülich, Germany*
[2]*Helmholtz-Institut für Strahlen- und Kernphysik and Bethe Center for Theoretical Physics, Universität Bonn, D-53115 Bonn, Germany*
[3]*School of Physics, Nankai University, Tianjin 300071, China*
[4]*King Fahd University of Petroleum and Minerals (KFUPM), 31261 Dhahran, Saudi Arabia*
[5]*Faculty of Natural Sciences and Engineering, Gaziantep Islam Science and Technology University, Gaziantep 27010, Turkey*
[6]*Peng Huanwu Collaborative Center for Research and Education, International Institute for Interdisciplinary and Frontiers, Beihang University, Beijing 100191, China*

We present an *ab initio* study of the charge and matter radii of oxygen isotopes from ^{16}O to ^{20}O using nuclear lattice effective field theory (NLEFT) with high-fidelity N^3LO chiral interactions. To efficiently address the Monte Carlo sign problem encountered in nuclear radius calculations, we introduce the *partial pinhole algorithm*, significantly reducing statistical uncertainties and extending the reach to more neutron-rich and proton-rich isotopes. Our computed charge radii for ^{16}O, ^{17}O, and ^{18}O closely match experimental data, and we predict a charge radius of 2.810(32) fm for ^{20}O. The calculated matter radii show excellent agreement with values extracted from low-energy proton and electron elastic scattering data, but are inconsistent with those derived from interaction cross sections and charge-changing cross section measurements. These discrepancies highlight model-dependent ambiguities in the experimental extraction methods of matter radii and underscore the value of precise theoretical benchmarks from NLEFT calculations.

Introduction—The nuclear radius, which characterizes the size of the nucleus, is one of the most fundamental properties of atomic nuclei. With the advancement of experimental techniques, there has been a rapid increase in available data on nuclear charge and matter radii for both stable and unstable isotopes [1–4]. On the one hand, these data have significantly enhanced our understanding of nuclear structure, revealing novel phenomena such as nuclear halos [5,6], neutron skins [7,8], and nuclear shape phase transitions [9,10]. On the other hand, they pose considerable challenges to nuclear theory, particularly to *ab initio* approaches.

Despite the remarkable progress in nuclear theory, achieving accurate descriptions of nuclear charge radii remains a significant challenge [11–17]. A notable example is the oxygen isotope chain. Most *ab initio* calculations underestimate the charge radius of ^{16}O by roughly 7–15%

[11,18]. Furthermore, while ^{16}O and ^{17}O exhibit similar charge radii, a pronounced increase in the charge radius is observed experimentally for ^{18}O in comparison to ^{16}O and ^{17}O [1]. To our knowledge, this intriguing feature is not captured by any existing theoretical approach. Although the chiral interaction $NNLO_{sat}$ successfully reproduces the charge radius of ^{16}O by including it among the fitted observables [18], it still fails to give the substantial increase seen in ^{18}O [13,16].

Nuclear lattice effective field theory (NLEFT) [19,20] offers a different perspective on this problem. Recently, the wave function matching method [21] was proposed to mitigate the notorious Monte Carlo sign problem in the imaginary-time evolution of quantum many-body simulations, which introduces strong cancellations between positive and negative amplitudes. In combination with high-fidelity N^3LO chiral interactions, the binding energies of both light and medium-mass nuclei up to $A = 58$ are well reproduced. While charge radii are generally well described, including the pronounced increase in ^{18}O compared to $^{16,17}O$, they are often accompanied by significantly larger statistical uncertainties. This is largely due to the commonly used pinhole algorithm, which inserts an A-body density operator during the imaginary-time evolution [22]. This insertion leads to unpaired nucleons, which results in additional strong sign oscillations, particularly for nuclei with larger mass numbers and/or pronounced

---

*Contact author: zxren@nankai.edu.cn
†Contact author: selhatisari@gmail.com
‡Contact author: meissner@hiskp.uni-bonn.de

proton-neutron asymmetry, thereby complicating the investigation of subtle isotopic trends in nuclear radii.

In this Letter, we propose an extension of the pinhole algorithm, referred to as the *partial pinhole algorithm*, that reduces the rank of the many-body density operator in order to mitigate the sign problem in nuclear radius calculations within the framework of NLEFT. This reduced operator is implemented via the recently developed rank-operator method [23]. We combine the partial pinhole algorithm with the wave function matching method using high-fidelity N^3LO chiral interactions. As a first application, we investigate both charge and matter radii of a number of oxygen isotopes.

Formalism—The full details of our lattice calculations are shown in Supplemental Material [24]. To illustrate the idea of the partial pinhole algorithm and how it is combined with NLEFT in calculating nuclear radii, we adopt a simplified Hamiltonian with an attractive two-body contact short range interaction ($C < 0$),

$$H = K + \frac{1}{2}C\sum_{\boldsymbol{n}}:\rho^2(\boldsymbol{n}):, \tag{1}$$

where K is the kinetic energy term with nucleon mass $m = 938.9$ MeV, the colons indicate normal ordering, and $\rho(\boldsymbol{n}) = \sum_{\sigma\tau}\rho_{\sigma\tau}(\boldsymbol{n}) = \sum_{\sigma\tau}a^\dagger_{\sigma\tau}(\boldsymbol{n})a_{\sigma\tau}(\boldsymbol{n})$. Here, $\rho_{\sigma\tau}(\boldsymbol{n})$ is the one-body density operator at lattice site $\boldsymbol{n}$ for spin σ and isospin τ.

The ground state wave functions of H can be obtained by applying imaginary time projectors to a trial wave function Ψ_0, $|\Psi\rangle = \lim_{\tau\to\infty}e^{-H\tau/2}|\Psi_0\rangle$. In Monte Carlo simulations, τ is divided into L_t slices with temporal spacing a_t such that $\tau = L_ta_t$. For each time slice, the two-body interaction is defined as nucleons propagated in a fluctuating background auxiliary field using a Hubbard-Stratonovich transformation,

$$\exp\left(-\frac{a_tC}{2}\rho^2\right) = \sqrt{\frac{1}{2\pi}}\int ds\,\exp\left(-\frac{s^2}{2} + \sqrt{-a_tC}s\rho\right), \tag{2}$$

where s is the auxiliary field at a lattice site. Therefore, the wave function $|\Psi\rangle$ can be written as an auxiliary field path-integral expression,

$$|\Psi\rangle = \int \mathcal{D}s_1\cdots\mathcal{D}s_{L_t/2}M(s_{L_t/2})\cdots M(s_1)|\Psi_0\rangle, \tag{3}$$

where the initial wave function $|\Psi_0\rangle$ is an A-nucleon Slater determinant, such as alpha clusters states or shell-model wave functions, and the normal-ordered transfer matrix M is defined as

$$M(s_{n_t}) = \,:\exp\left[-a_tK + \sqrt{-a_tC}\sum_{\boldsymbol{n}}s_{n_t}(\boldsymbol{n})\rho(\boldsymbol{n})\right]:. \tag{4}$$

Therefore, $|\Psi\rangle$ is expressed as a linear combination of A-nucleon Slater determinants, each of which is associated with a specific configuration of auxiliary fields $\vec{s}$.

With the wave function $|\Psi\rangle$ in Eq. (3), the root-mean-square (RMS) point-proton radius of a nucleus with proton number Z, neutron number N, and mass number A can be evaluated by

$$\langle r_p^2\rangle = \frac{1}{Z}\sum_{\boldsymbol{n},\sigma,\tau=p}\langle\rho_{\sigma\tau}(\boldsymbol{n})(\boldsymbol{n}-\hat{\boldsymbol{r}}_{\text{c.m.}})^2\rangle, \tag{5}$$

where $\hat{\boldsymbol{r}}_{\text{c.m.}} = \sum_{\boldsymbol{n},\sigma,\tau}\boldsymbol{n}\rho_{\sigma\tau}(\boldsymbol{n})/A$ is the center-of-mass operator. The expression can be rewritten in terms of a set of two-body correlation functions $G_{\alpha\beta}$ as

$$\langle r_p^2\rangle = \frac{N}{ZA^2}G_{pp} + \frac{N-Z}{ZA^2}G_{pn} - \frac{1}{A^2}G_{nn}, \tag{6}$$

with

$$G_{\alpha\beta} = \sum_{\substack{\boldsymbol{n}_1,\sigma_1,\tau_1=\alpha \\ \boldsymbol{n}_2,\sigma_2,\tau_2=\beta}}\langle:\rho_{\sigma_1\tau_1}(\boldsymbol{n}_1)\rho_{\sigma_2\tau_2}(\boldsymbol{n}_2):\rangle(\boldsymbol{n}_1-\boldsymbol{n}_2)^2. \tag{7}$$

Similarly, the matter radius is given by

$$\langle r_m^2\rangle = \frac{1}{A}\sum_{\boldsymbol{n},\sigma,\tau}\langle\rho_{\sigma\tau}(\boldsymbol{n})(\boldsymbol{n}-\hat{\boldsymbol{r}}_{\text{c.m.}})^2\rangle$$
$$= \frac{1}{2A^2}G_{pp} + \frac{1}{A^2}G_{pn} + \frac{1}{2A^2}G_{nn}. \tag{8}$$

Thus, nuclear radii can be expressed in terms of just three two-body correlation functions. It is important to note that since the matter radius corresponds to the second radial moment of the intrinsic nuclear density distribution (or equivalently, the squared nuclear wave function), its numerical value is sensitive to both the theoretical framework used and the specific methods adopted when extracting it from experimental observables.

Similar to the previous studies on computing the RMS charge radii [18,21,25], we use the standard relation [26]

$$r_{\text{ch}}^2 = \langle r_p^2\rangle + R_p^2 + \frac{N}{Z}R_n^2 + \frac{3}{4m_p^2}, \tag{9}$$

where $R_p^2 = 0.7056$ fm^2 [27,28], $R_n^2 = -0.105$ fm^2 [29], and $m_p = 938.27$ MeV. Relativistic spin-orbit corrections and two-nucleon current contributions are not included in this work.

A direct calculation of the correlation functions $G_{\alpha\beta}$ is computationally expensive, especially when the corrections from high-fidelity chiral interactions are included

perturbatively. To evaluate them more efficiently, we introduce the *partial pinhole algorithm*. We define a normal-ordered M-body density operator,

$$\rho_M(\vec{c}) = \; :\rho_{\sigma_1\tau_1}(\boldsymbol{n}_1)\cdots\rho_{\sigma_M\tau_M}(\boldsymbol{n}_M):, \qquad (10)$$

using the notation $\vec{c} = (c_1, ..., c_M)$. Here, $c_i = (\boldsymbol{n}_i, \sigma_i, \tau_i)$ specifies the quantum numbers of the ith density operator, with $\boldsymbol{n}_i$ denoting the lattice coordinate, and σ_i and τ_i representing spin and isospin. The summation over $\vec{c}$ satisfies

$$\sum_{\vec{c}}\rho_M(\vec{c}) = \hat{N}(\hat{N} - 1)\cdots(\hat{N} - M + 1)$$

$$= A(A - 1)\cdots(A - M + 1), \qquad (11)$$

where $\hat{N}$ is the particle-number operator. The equality of the second line stems from the fact that we are working in A-nucleon subspace. Therefore, this summation is proportional to the identity operator.

The correlation functions $G_{\alpha\beta}$ can then be evaluated as

$$G_{\alpha\beta} = \frac{A(A - 1)}{M(M - 1)}$$
$$\times \frac{\sum_{\vec{c}}\left[\langle\Psi|\rho_M(\vec{c})|\Psi\rangle \sum_{i<j}\delta_{\tau_i\alpha}\delta_{\tau_j\beta}(\boldsymbol{n}_i - \boldsymbol{n}_j)^2\right]}{\sum_{\vec{c}}\langle\Psi|\rho_M(\vec{c})|\Psi\rangle}. \qquad (12)$$

The details about computing $(\boldsymbol{n}_i - \boldsymbol{n}_j)^2$ are presented in Supplemental Material [24]. Unlike the standard pinhole algorithm [22], the value of M is much smaller than the total number of nucleons A. As a result, ρ_M is no longer a projection operator, and acting with ρ_M on a single A-nucleon Slater determinant yields a linear combination of multiple A-nucleon Slater determinants.

Since $\rho_{\sigma\tau}(\boldsymbol{n})$ is a rank-one operator, that is, $:\rho_{\sigma\tau}^2(\boldsymbol{n}): = 0$, the rank-one operator method [23] allows us to express $\rho_M(\vec{c})$ as

$$\rho_M(\vec{c}) = \frac{1}{\varepsilon^M} : \exp[\varepsilon\rho_{\sigma_1\tau_1}(\boldsymbol{n}_1) + \cdots + \varepsilon\rho_{\sigma_M\tau_M}(\boldsymbol{n}_M)]: \qquad (13)$$

with $\varepsilon \to \infty$. It consists of a string of one-body operators which can be applied directly to each single-particle wave function in the Slater determinant.

The summations over $\vec{c}$ in Eq. (12) and the path integral over $\vec{s}$ in Eq. (3) are evaluated via Monte Carlo importance sampling. We generate an ensemble of $\vec{c}$, $\vec{s}$ configurations according to the relative probability weight,

$$P(\vec{c}, \vec{s}) = |\langle\Psi_0|M(s_{L_t})\cdots M(s_{L_t/2+1})\rho_M(\vec{c})$$
$$\times M(s_{L_t/2})\cdots M(s_1)|\Psi_0\rangle|. \qquad (14)$$

The strings of transfer matrices are generated by updating the auxiliary fields $\vec{s}$ using the shuttle algorithm [30]. At the middle time slice, the auxiliary field updates are paused, and the pinhole configuration $\vec{c}$ is updated by performing standard Metropolis accept/reject steps. Specifically, to update $\vec{c}$, we randomly select an index i in ρ_M and either move it to a neighboring site,

$$c_i = \{\boldsymbol{n}_i, \sigma_i, \tau_i\} \to c_i' = \{\boldsymbol{n}_i', \sigma_i, \tau_i\}, \qquad (15)$$

or reassign its spin and isospin,

$$c_i = \{\boldsymbol{n}_i, \sigma_i, \tau_i\} \to c_i' = \{\boldsymbol{n}_i, \sigma_i', \tau_i'\}. \qquad (16)$$

The new configuration $\vec{c}'$ is accepted if

$$P(\vec{c}', \vec{s})/P(\vec{c}, \vec{s}) > r, \qquad (17)$$

where the random number r is uniformly distributed between 0 and 1.

In this work, we combine the partial pinhole algorithm with the wave function matching method. The original chiral Hamiltonian is unitarily transformed into a new high-fidelity Hamiltonian H, whose wave function matches that of a computationally simple Hamiltonian, H_S, at a given radius. This ensures rapid convergence of the perturbative expansion in $H - H_S$. The details can be found in Ref. [21]. The formalism for applying the partial pinhole algorithm in perturbative calculations is provided in [24].

Results and discussion—In the following calculations, we adopt the N³LO chiral interactions from Ref. [21]. We also use a minimal sets of three-body force terms, where, in addition to nuclear binding energies, the charge radius of ⁴He is used to determine the low-energy constants (LECs) [31]. Although the number of involved free LECs is reduced from eight to six, the overall description of nuclear binding energies is similar to Ref. [21], as detailed in [24]. Our simulations are performed with a spatial lattice spacing of $a = 1.32$ fm, corresponding to a momentum cutoff $\Lambda = \pi/a \approx 471$ MeV. Additionally, we use a temporal lattice spacing of $a_t = 0.001$ MeV^{-1} and a cubic box of length $L = 13.2$ fm. Since the radii of the oxygen isotopes under investigation are all below 3 fm, this box size is clearly sufficient to suppress finite-volume effects.

In the partial pinhole algorithm, although one could in principle take $M = 2$ for ρ_M in Eq. (10) as the correlation functions $G_{\alpha\beta}$ in Eq. (7) are two-body observables, such a choice suffers from low computational efficiency. To improve sampling efficiency, we aim for each configuration $\vec{c}$ to contribute simultaneously to all three types of correlations: G_{pp}, G_{pn}, and G_{nn}. This requirement implies that the isospin indices in ρ_M must include at least two protons and two neutrons. We therefore adopt $M = 4$ and fix half of the indices to be protons and the other half to be neutrons in our calculations. We have further verified that the final results are largely insensitive to the specific choice of M, having tested $M = 4, 6, 8$, and 10 [24].
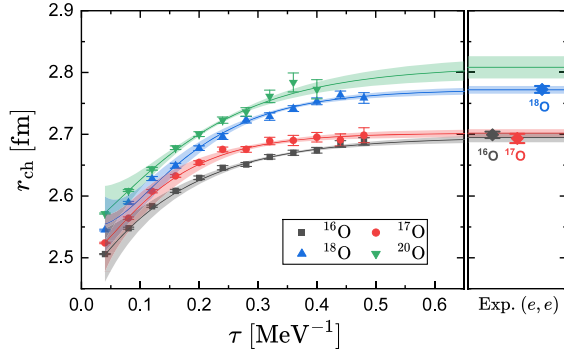
FIG. 1. Left: charge radii of oxygen isotopes calculated using the partial pinhole algorithm with the N^{3}LO interaction as functions of the projection time τ. The black squares, red circles, blue upward triangles, and green downward triangles represent the results for ^{16}O, ^{17}O, ^{18}O, and ^{20}O, respectively. The solid lines denote fits using a double-exponential function, with the shaded bands indicating the 1σ uncertainties. Right: diamonds indicate the charge radii deduced from electron scattering data for ^{16}O (black), ^{17}O (red), and ^{18}O (blue). Horizontal lines represent the extrapolated values at $\tau \to \infty$ from the left panel, with shaded bands showing the 1σ uncertainties.

In [24], we benchmark the charge radii of ^{16}O and ^{17}O using both the standard pinhole and the partial pinhole algorithms with the simple Hamiltonian H_S. Although we find that both methods yield consistent charge radii, the partial pinhole algorithm maintains a significantly larger average phase factor and substantially reduces statistical uncertainties, particularly in the case of ^{17}O. This improvement becomes even more substantial for heavier nuclei such as ^{40}Ca, and is further amplified when applying the full N^{3}LO chiral interactions.

Figure 1 shows the charge radii of ^{16}O, ^{17}O, ^{18}O, and ^{20}O calculated using the partial pinhole algorithm together with the chiral interactions at N^{3}LO, where a specified set of three-body forces is adopted [24]. Due to the substantial suppression of the sign oscillations, we are now able to reach significantly larger imaginary times as compared to earlier works. For ^{16}O, ^{17}O, and ^{18}O, the calculated radii exhibit a clear exponential decay behavior. A double-exponential fit is used to account for residual excited-state contamination and extrapolate the results to $\tau \to \infty$; see Supplemental Material [24] for details. The uncertainties of the extrapolation are quantified using the covariance matrix obtained from the nonlinear fit. The extrapolated charge radii at $\tau \to \infty$ are 2.695(8), 2.702(7), and 2.772(6) fm, respectively. Compared to the corresponding results presented in Ref. [21], the 1σ uncertainties are significantly reduced. This substantial improvement in precision enables a detailed investigation of the subtle isotopic trend in the charge radii of oxygen isotopes. This level of precision also makes it feasible to probe smaller effects such as relativistic spin-orbit corrections and two-nucleon currents in the

TABLE I. The charge and matter radii (units are fm) calculated by the partial pinhole algorithm using the N^{3}LO interaction, where the theoretical uncertainties are estimated using ten sets of three-nucleon forces. The available experiment data (Exp.) are also given for comparison. Exp. (e, e) [1]: charge radii deduced from electron scattering data. Exp. (e, e), (p, p) [13]: matter radii deduced from electron scattering and proton scattering data. Exp. σ_I [2]: matter radii deduced from interaction cross sections. Exp. σ_{cc} [16]: matter radii deduced from charge changing cross sections.

	^{16}O	^{17}O	^{18}O	^{20}O
r_{ch} [NLEFT]	2.704(17)	2.709(15)	2.768(17)	2.810(32)
Exp. (e, e)	2.699(5)	2.693(8)	2.776(2)	
r_m [NLEFT]	2.576(17)	2.651(14)	2.744(19)	2.863(33)
Exp. (e, e), (p, p)	2.60(8)	2.67(10)	2.77(10)	2.90(10)
Exp. σ_I	2.54(2)	2.59(5)	2.61(8)	2.69(3)
Exp. σ_{cc}	2.57(2)		2.64(8)	2.71(3)

future. For ^{20}O, however, the stronger sign problem arising from its larger proton-neutron asymmetry prevents the simulation from reaching very large projection times, and the extrapolation is terminated at $\tau = 0.4$ MeV^{-1}. As a result, the extrapolated charge radius exhibits a larger uncertainty.

The extrapolated charge radii are summarized in Table I, where results using nine additional sets of three-nucleon forces are included to estimate theoretical uncertainties [31]. Note that the central values and the corresponding errors are shifted compared to the extrapolated ones in Fig. 1. The results show that ^{16}O and ^{17}O have very similar charge radii, while ^{18}O exhibits a noticeable increase, consistent with experimental data [1]. We note that, although ^{16}O is commonly described as a spherical doubly magic nucleus within shell-model-based approaches, NLEFT simulations predict a distinct tetrahedral arrangement of alpha clusters [32]. Similar alpha-cluster structures in ^{8}Be [33], ^{12}C [34], and ^{20}Ne [35] have also been predicted by NLEFT in their ground states. Supporting this picture, previous NLEFT studies [34] demonstrated that the ground state of ^{12}C robustly converges to an equilateral triangular arrangement of alpha clusters independent of the choice of the initial state. By analogy, assuming that ^{16}O similarly forms a stable tetrahedral cluster configuration as indicated by NLEFT calculations, this intrinsic clustering could explain the success of NLEFT in reproducing oxygen isotope charge radii.

We also compute the matter radii of oxygen isotopes using the partial pinhole algorithm. The results for ^{16}O, ^{17}O, ^{18}O, and ^{20}O are shown in Fig. 2. Similar to the charge radii shown in Fig. 1, we perform a double-exponential fit to extrapolate the data to $\tau \to \infty$; see [24] for details. In contrast to the charge radii, the matter radii increase monotonically with mass number. The extrapolated matter
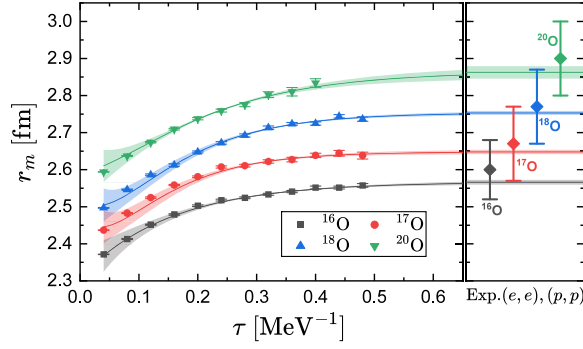
FIG. 2. Left: matter radii of oxygen isotopes calculated using the partial pinhole algorithm with the N^3LO interaction as functions of the projection time τ. The black squares, red circles, blue upward triangles, and green downward triangles represent the results for ^{16}O, ^{17}O, ^{18}O, and ^{20}O, respectively. The solid lines denote fits using a double-exponential function, with the shaded bands indicating the 1σ uncertainties. Right: diamonds indicate the matter radii deduced from electron scattering and proton scattering data for ^{16}O (black), ^{17}O (red), ^{18}O (blue), and ^{20}O (green). Horizontal lines represent the extrapolated values at $\tau \to \infty$ from the left panel, with shaded bands showing the 1σ uncertainties.

radii are listed in Table I, along with values obtained using nine additional sets of three-nucleon forces [31].

In Table I, we also compare our results with experimental matter radii extracted from electron and proton scattering [(e, e) and (p, p)] [13], interaction cross sections (σ_I) [2], and charge-exchange cross sections (σ_{cc}) [16]. Unlike charge radii, the extraction of matter radii often involves some degree of model dependence, leading to discrepancies among different experimental methods. For example, matter radii derived from low-energy proton elastic scattering tend to be systematically larger than those extracted from σ_I and σ_{cc} measurements. The most notable case is ^{20}O, where differences up to 0.2 fm are observed among the three different measurements. As discussed in Ref. [13], the (e, e) and (p, p) data provide a more reliable descriptions, since the correlations in the target are usually not included in the other methods. From Table I, we can find our calculated matter radii agree well with the values extracted from (e, e) and (p, p) data, and thus support the statement given in Ref. [13].

Summary and perspectives—We have performed an *ab initio* calculation of the charge and matter radii of oxygen isotopes from ^{16}O to ^{20}O using nuclear lattice effective field theory (NLEFT) with the high-fidelity N^3LO chiral interactions. To mitigate the Monte Carlo sign problem in nuclear radius calculations, we introduce the *partial pinhole algorithm*, which reduces the rank of the many-body density operator in the standard pinhole approach and significantly lowers the statistical uncertainties. This method enables access to much larger projection times and extends the applicability to more neutron-rich and proton-rich nuclei. Our results accurately reproduce the experimental charge radii of ^{16}O, ^{17}O, and ^{18}O, demonstrating the capability of NLEFT in describing nuclear structure properties. The charge radius of ^{20}O is predicted to be 2.810 (32) fm. The calculated matter radii show excellent agreement with values extracted from low-energy electron and proton scattering, while deviating from those inferred from interaction and charge-exchange cross sections. These results underscore the need for further experimental clarification, particularly for neutron-rich isotopes, with improved precision and reduced model dependence.

As a general and versatile method, the partial pinhole algorithm holds broad potential future applications. It can be integrated with other Monte Carlo techniques, such as the perturbative quantum Monte-Carlo method [36], and has already been successfully applied to the calculation of additional observables, including electromagnetic transitions [33]. Its ability to suppress sign oscillations while maintaining high accuracy suggests wide applicability not only across nuclear systems, but also to broader classes of quantum many-body problems.

Data availability—The data supporting this study's findings are available within the article.

[1] I. Angeli and K. P. Marinova, At. Data Nucl. Data Tables **99**, 69 (2013).

[2] A. Ozawa, O. Bochkarev, L. Chulkov, D. Cortina, H. Geissel, M. Hellstrom, M. Ivanov, R. Janik, K. Kimura, T. Kobayashi *et al.*, Nucl. Phys. **A691**, 599 (2001).

[3] P. Campbell, I. D. Moore, and M. R. Pearson, Prog. Part. Nucl. Phys. **86,** 127 (2016).

[4] X. F. Yang, S. J. Wang, S. G. Wilkins, and R. F. Garcia Ruiz, Prog. Part. Nucl. Phys. **129,** 104005 (2023).

[5] I. Tanihata, H. Hamagaki, O. Hashimoto, Y. Shida, N. Yoshikawa, K. Sugimoto, O. Yamakawa, T. Kobayashi, and N. Takahashi, Phys. Rev. Lett. **55,** 2676 (1985).

[6] R. Kanungo, W. Horiuchi, G. Hagen, G. R. Jansen, P. Navratil, F. Ameil, J. Atkinson, Y. Ayyad, D. Cortina-Gil, I. Dillmann et al., Phys. Rev. Lett. **117,** 102501 (2016).

[7] D. Adhikari et al. (PREX Collaboration), Phys. Rev. Lett. **126,** 172502 (2021).

[8] D. Adhikari et al. (CREX Collaboration), Phys. Rev. Lett. **129,** 042501 (2022).

[9] B. A. Marsh, T. Day Goodacre, S. Sels, Y. Tsunoda, B. Andel, A. N. Andreyev, N. A. Althubiti, D. Atanasov, A. E. Barzakh, J. Billowes et al., Nat. Phys. **14,** 1163 (2018); **18,** 219(E) (2022).

[10] J. G. Cubiss, A. N. Andreyev, A. E. Barzakh, P. Van Duppen, S. Hilaire, S. Péru, S. Goriely, M. Al Monthery, N. A. Althubiti, B. Andel et al., Phys. Rev. Lett. **131,** 202501 (2023).

[11] A. Cipollone, C. Barbieri, and P. Navrátil, Phys. Rev. C **92,** 014306 (2015).

[12] R. F. Garcia Ruiz, M. L. Bissell, K. Blaum, A. Ekström, N. Frömmgen, G. Hagen, M. Hammen, K. Hebeler, J. D. Holt, G. R. Jansen et al., Nat. Phys. **12,** 594 (2016).

[13] V. Lapoux, V. Somà, C. Barbieri, H. Hergert, J. D. Holt, and S. R. Stroberg, Phys. Rev. Lett. **117,** 052501 (2016).

[14] A. J. Miller, K. Minamisono, A. Klose, D. Garand, C. Kujawa, J. D. Lantis, Y. Liu, B. Maaß, P. F. Mantica, W. Nazarewicz, W. Nörtershäuser, S. V. Pineda, P. G. Reinhard, D. M. Rossi, F. Sommer, C. Sumithrarachchi, A. Teigelhöfer, and J. Watkins, Nat. Phys. **15,** 432 (2019).

[15] Á. Koszorús, X. F. Yang, W. G. Jiang, S. J. Novario, S. W. Bai, J. Billowes, C. L. Binnersley, M. L. Bissell, T. E. Cocolios, B. S. Cooper et al., Nat. Phys. **17,** 439 (2021); **17,** 539(E) (2021).

[16] S. Kaur, R. Kanungo, W. Horiuchi, G. Hagen, J. D. Holt, B. S. Hu, T. Miyagi, T. Suzuki, F. Ameil, J. Atkinson et al., Phys. Rev. Lett. **129,** 142502 (2022).

[17] K. König, S. Fritzsche, G. Hagen, J. D. Holt, A. Klose, J. Lantis, Y. Liu, K. Minamisono, T. Miyagi, W. Nazarewicz et al., Phys. Rev. Lett. **131,** 102501 (2023).

[18] A. Ekström, G. R. Jansen, K. A. Wendt, G. Hagen, T. Papenbrock, B. D. Carlsson, C. Forssén, M. Hjorth-Jensen, P. Navrátil, and W. Nazarewicz, Phys. Rev. C **91,** 051301 (2015); **109,** 059901(E) (2024).

[19] D. Lee, Prog. Part. Nucl. Phys. **63,** 117 (2009).

[20] T. A. Lähde and U.-G. Meißner, Nuclear Lattice Effective Field Theory: An Introduction, Lecture Notes in Physics Vol. 957 (Springer, New York, 2019).

[21] S. Elhatisari, L. Bovermann, Y. Z. Ma, E. Epelbaum, D. Frame, F. Hildenbrand, M. Kim, Y. Kim, H. Krebs, T. A. Lähde et al., Nature (London) **630,** 59 (2024).

[22] S. Elhatisari, E. Epelbaum, H. Krebs, T. A. Lähde, D. Lee, N. Li, B.-N. Lu, U.-G. Meißner, and G. Rupak, Phys. Rev. Lett. **119,** 222505 (2017).

[23] Y. Z. Ma, Z. Lin, B. N. Lu, S. Elhatisari, D. Lee, N. Li, U.-G. Meißner, A. W. Steiner, and Q. Wang, Phys. Rev. Lett. **132,** 232502 (2024).

[24] See Supplemental Material at http://link.aps.org/supplemental/10.1103/y6s2-43ym for details of the lattice Hamiltonian, perturbation formalism for the partial pinhole algorithm, the distance between two lattice sites, benchmark with simple Hamiltonian H_S, and imaginary time extrapolation.

[25] X. X. Sun, H. Le, U.-G. Meißner, and A. Nogga, Phys. Rev. C **112,** 024317 (2025).

[26] J. Friar and J. Negele, in Advances in Nuclear Physics, edited by M. Baranger and E. Vogt (Springer US, New York, 1975), pp. 219–376.

[27] R. Pohl, A. Antognini, F. Nez, F. D. Amaro, F. Biraben, J. M. R. Cardoso, D. S. Covita, A. Dax, S. Dhawan, L. M. P. Fernandes et al., Nature (London) **466,** 213 (2010).

[28] Y. H. Lin, H. W. Hammer, and U.-G. Meißner, Phys. Rev. Lett. **128,** 052002 (2022).

[29] A. A. Filin, D. Möller, V. Baru, E. Epelbaum, H. Krebs, and P. Reinert, Phys. Rev. C **103,** 024313 (2021).

[30] B.-N. Lu, N. Li, S. Elhatisari, D. Lee, E. Epelbaum, and U.-G. Meißner, Phys. Lett. B **797,** 134863 (2019).

[31] S. Elhatisari et al. (to be published).

[32] E. Epelbaum, H. Krebs, T. A. Lähde, D. Lee, U.-G. Meißner, and G. Rupak, Phys. Rev. Lett. **112,** 102501 (2014).

[33] S. Shen, S. Elhatisari, D. Lee, U.-G. Meißner, and Z. Ren, Phys. Rev. Lett. **134,** 162503 (2025).

[34] S. Shen, S. Elhatisari, T. A. Lähde, D. Lee, B. N. Lu, and U.-G. Meißner, Nat. Commun. **14,** 2777 (2023).

[35] E. Harris, M. Barbui, J. Bishop, G. Chubarian, S. Konig, E. Koshchiy, K. D. Launey, D. Lee, Z. Luo, Y. Z. Ma et al., arXiv:2507.17059 [nucl-ex].

[36] B. N. Lu, N. Li, S. Elhatisari, Y. Z. Ma, D. Lee, and U.-G. Meißner, Phys. Rev. Lett. **128,** 242501 (2022).

[37] www.gauss-centre.eu

[38] https://www.nhr-verein.de/en/our-partners